MASSACHUSETTS INSTITUTE OF TECHNOLOGY
NOV 13 2008
LIBRARIES

Simulation of tongue muscle deformation

by

Alvin Y. Liang

Submitted to the Department of Electrical Engineering and Computer Science in Partial Fulfillment of the Requirements for the Degree of Master of Engineering in Electrical Engineering and Computer Science at the Massachusetts Institute of Technology

August 2008

Copyright 2008 Massachusetts Institute of Technology.

All rights reserved.

Author _____

Department of Electrical Engineering and Computer Science

August 22, 2008

Certified by _____

Richard Gilbert, M.D.

Thesis Supervisor

Accepted by _____

Arthur C. Smith

Professor of Electrical Engineering

Chairman, Department Committee on Graduate Theses

ARCHIVES

Simulation of tongue muscle deformation

by

Alvin Y. Liang

Submitted to the Department of Electrical Engineering and Computer Science

on August 22, 2008 in Partial Fulfillment of the Requirements

for the Degree of Master of Engineering in Electrical Engineering and Computer Science

Abstract

The tongue is an intricately configured muscular organ that undergoes a stereotypical set of deformations during the course of normal human swallowing. The tongue's myoarchitecture consists of a large array of variably aligned and extensively interwoven intrinsic and extrinsic muscles. To elucidate the explicit relationship between 3D aligned lingual fiber organization and mechanics during physiological deformations, we performed finite element modeling (FEM) employing a mesh generated from mesoscale multivoxel fiber like tracts obtained in vivo by high resolution diffusion tensor imaging with tractography. DTI tractography displayed the complete fiber anatomy of the tongue, consisting of a core region of orthogonally aligned fibers encased within a longitudinal sheath, which merge with the externally connected styloglossus, hyoglossus, and genioglossus fibers.

1 Background

The tongue is an intricately configured muscular organ, which is responsible for the manipulation and transport of food in the oral cavity during swallowing, as well as the subtle variations in shape and stiffness needed for human speech. One of the unique properties of the tongue is that it is a muscular hydrostat. A muscular hydrostat has a high water content that in turn makes it relatively incompressible, allowing it to change physical conformation without a change in volume. (For a review of the tongue as muscular hydrostat, see Gilbert *et al.* 2007.)

The tongue's exquisite mechanical virtuosity is closely linked with the complexity of its myoarchitecture. Lingual myoarchitecture consists of a large array of variably aligned and extensively interwoven intrinsic (without attachment to bony surfaces) and extrinsic (with attachment to bony surfaces) muscles. The intrinsic musculature consists of a core region of orthogonally-aligned fibers, contained within a sheath-like bundle of longitudinally oriented fibers. The intrinsic fibers are delicately merged with extrinsic muscles that modify shape and position from a superior direction (palatoglossus), posterior direction (styloglossus), and inferior direction (genioglossus and hyoglossus). It can be argued that the mammalian tongue's hydrostatic properties can be attributed to its orthogonally aligned fibers.

In general, the direction of skeletal muscle contraction is determined by the orientation of these muscle fibers. In some tissues, such as those of the extremities, the principal fiber direction is easily determined, since the fibers are basically aligned along a

single axis. However, in the tongue, we have seen that fibers are aligned along multiple axes. Accurately mapping lingual muscle fiber orientation has previously relied on laborious dissection and histological approaches. One disadvantage of these classical methods is that they are inherently two-dimensional in nature and cannot resolve fibers coming in and out of the plane easily (McLean and Prothero, 1987; McLean and Prothero, 1992). More recently, diffusion magnetic resonance imaging (MRI) (Stejskal, 1965) has been used to visualize lingual myoarchitecture in situ. This advance has allowed resolution of more complex fiber patterns at multiple scales, in three-dimensions, and *in situ*.

Diffusion weighted imaging has the capacity to resolve anisotropic particle movement, and thus infer fiber organization at a voxel scale in biological tissue. Our group has also demonstrated anisotropy of water diffusion in the setting of lingual skeletal muscle for excised tissue and in vivo, and have anatomically validated these representations through correlation with whole tissue 3D microscopy. More recent work from our group combined diffusion tensor imaging with tractography to produce three-dimensional images of lingual myoarchitecture (Gaige et al 2007). Moreover, we have demonstrated that mesoscale tractography approximates the alignment of local strain rate vectors associated with lingual deformation during the course of water bolus swallows (Felton et al 2008).

Even with the advances in imaging technologies, it is still difficult to relate muscle anatomy to muscle function in a quantitative manner. For example, which muscles in the tongue are used during swallowing? How hard does each muscle contract? At what point in time during the act of swallowing does each muscle contract? The ability to relate the

deformation of mesoscale myofiber tracts to physiological patterns of tissue deformation should improve our understanding of multi-scale mechanical relationships existing among the structurally complex regions of the tongue and allow us to answer these questions. However, developing such a relation requires the development of a practical finite element simulation of human lingual deformation based on the tongue's underlying myoarchitecture.

There has been much work done to incorporate anatomical knowledge into finite element representations that produce local deformations approximating swallowing and speech deformation patterns. However, these simulations, despite utilizing a complex myoarchitecture, do not reflect or address the role of such myoarchitectures in producing hydrostatic deformation. Conversely, other models do address the idea of hydrostatic motion in the tongue, but are limited because they only describe a limited range of behavior or motion (Skierczynski *et al.*, 1996; Kristan *et al.*, 2000; Wilson *et al.*, 1991; Van Leeuwen and Kier, 1997), or do not account for external constraints and forces such as gravity, water drag (Wadepuhl and Beyn, 1989), or the isovolumeic property of hydrostats (Jordan, 1996). What almost all of these studies do reveal, however, is that many muscles work synergistically to produce lingual deformation. As an example, our group's previous results led to the hypothesis that the longitudinalis muscle contracts synergistically with the transversus to produce tongue bending (Napadow *et al.*, 2002).

In this work we provide the basis for a comprehensive mathematical model of tongue mechanics relating tongue myofiber architecture with the deformation of the tongue, utilizing recent advances in tractography to generate mesh for a finite element

model. We test our model by comparing to known deformations in the propulsive phase during the first 500 milliseconds of the swallowing action. Such a model is unique compared to previous models of lingual mechanics in that it is derived from measurable human myoarchitectural data and incorporates validated concepts of non-linear activation and neuromuscular control in skeletal muscle. Thus, our method is general and applicable to many different deformations and situations, and is capable of revealing the synergistic activation patterns of the various lingual myofiber groups. We hope this model can provide the basis for surgical planning tools and disease models in not only the tongue, but also in other organs for which myofiber tractography can reveal the complex, interwoven fiber patterns, such as the heart, rectum, and GI tract.

2 Overview of methods

The overall goal of this project was to determine how muscle fibers were activated in the tongue during the propulsive phase of swallowing. We provide an overview of the process here.

Before we describe the actual execution of the research, to understand what "activation" means, we provide some mathematical background in Section 3. In brief, we use a variant of the Hill's model for muscle, assuming that the muscles in the tongue contract in a manner similar to skeletal muscle. Muscles are activated via some internal signal; this activation is described by a mathematical function. We divide the gross muscle into individual mesoscopic elements. This is a finite element model, or FEM. In this model, each muscle element contracts according to its shape and directionality when activated. We iterate to get the results of these activations and resultant contractions over small periods of time. This contraction in turn leads to a gross deformation or displacement of the entire muscle.

So, the first step in determining the relationship between activation, anatomy, and deformation in the tongue would be to derive a detailed model of said tongue based directly on lingual anatomy. Specifically, we must derive an image of the myofiber architecture in the tongue. This is achieved using diffusion tensor imaging (DTI), which will be described in more detail in section 4. From the DTI image of the tongue, we use myofiber tractography to determine the length, position, and directionality of the

individual muscle fibers. Myofiber tractography yields a second image, from which take a midline slice.

This slice provides the basis for a two-dimensional FEM mesh. We derive a mesh that approximates the anatomical features described in the midline tractographic image slice. After deriving a mesh, we then apply activation functions and material properties to the mesh, and simulate the deformation caused by those activations. The assumptions behind our choices are key, and will be discussed at length. We attempt to find a set of activation functions that simulates the tongue movement described by the gated phase contrast MRI images produced by Felton *et al.* (2007, 2008).

3 Finite elements and the Hill's muscle model

3.1 Finite element method for muscle

3.1.1 Overview

In section 3 we describe the finite element algorithm and Hill's three-element muscle model used in our work. The bulk of the mathematics described in this section was previously described by Kojic et al. (1998). Skeletal muscles can be considered as mechanical structures that deform under both external loading and internal excitation. However, the stress-strain relation is non-linear, so the muscle mechanical system is also non-linear, even in the case of small deformation. Geometric non-linearities must also be considered. An example of such geometric non-linearity can be seen if one flexes his or her arm and observes the bicep: muscles can displace and deform greatly.

Because we are considering the muscle as a mechanical structure, we can use methods used in solid mechanics analysis to determine its mechanical response. The most common such method is the finite element method, where the muscle continuum is discretized. If we neglect inertial forces, we can determine muscle motion via an incremental-iterative scheme by forming the equilibrium equation for a given load step n and equilibrium iteration i (in the superscripts below) for that time step:

$$\left({}^{n+1}\mathbf{K}_L + {}^{n+1}\mathbf{K}_{NL}\right)^{(i-1)}\Delta\mathbf{U}^{(i)} = {}^{n+1}\mathbf{F}^{ext} - {}^{n+1}\mathbf{F}^{\mathrm{int}(i-1)} \qquad (3.1.1)$$

where ${}^{n+1}\mathbf{K}_L$ and ${}^{n+1}\mathbf{K}_{NL}$ are the geometrically linear and geometrically nonlinear stiffness matrices, $\Delta\mathbf{U}^{(i)}$ are the increments of nodal displacements; and ${}^{n+1}\mathbf{F}^{ext}$ and ${}^{n+1}\mathbf{F}^{\text{int}(i-1)}$ are the external and internal nodal force vectors.

In the next sections, we demonstrate the calculation of the stresses ${}^{n+1}\sigma^{i-1}$ and the tangent constitutive matrix ${}^{n+1}\mathbf{C}^{i-1}$ of stress-strain relations within the finite element. The following two expressions form the basis of this calculation. The internal force vector can be written as

$$ {}^{n+1}\mathbf{F}^{\text{int}(i-1)} = \int_{{}^{n+1}V^{(i-1)}} \left({}^{n+1}\mathbf{B}_L^T \, {}^{n+1}\sigma \right)^{(i-1)} dV \tag{3.1.2} $$

The linear stiffness matrix can be expressed as

$$ {}^{n+1}\mathbf{K}_L = \int_{{}^{n+1}V^{(i-1)}} \left({}^{n+1}\mathbf{B}_L^T \, {}^{n+1}\mathbf{C} \, {}^{n+1}\mathbf{B}_L \right)^{(i-1)} dV \tag{3.1.3} $$

In these equations, $\mathbf{B}$ represents the linear strain-displacement matrix, which contains derivatives of interpolation functions that approximate the displacement field within the element, and V is the element's volume.

Skeletal muscle has a fibrous structure; the fibers in a muscle generate the muscle force. Thus, we are primarily interested in stresses in the directions of muscle fibers. In figure 3.1.A, we have shown a finite element that represents a small portion of a muscle fiber whose direction is defined by the unit vector ξ_0. Stress $\sigma_{\xi\xi}$ in this direction depends on the elongation ΔL or stretch $\lambda = 1 + \Delta L / L_0$ of the fiber, and this dependence represents

the constitutive law for muscle. The constitutive law can be defined by an experimentally established model, such as Hill's model, which will be discussed shortly.

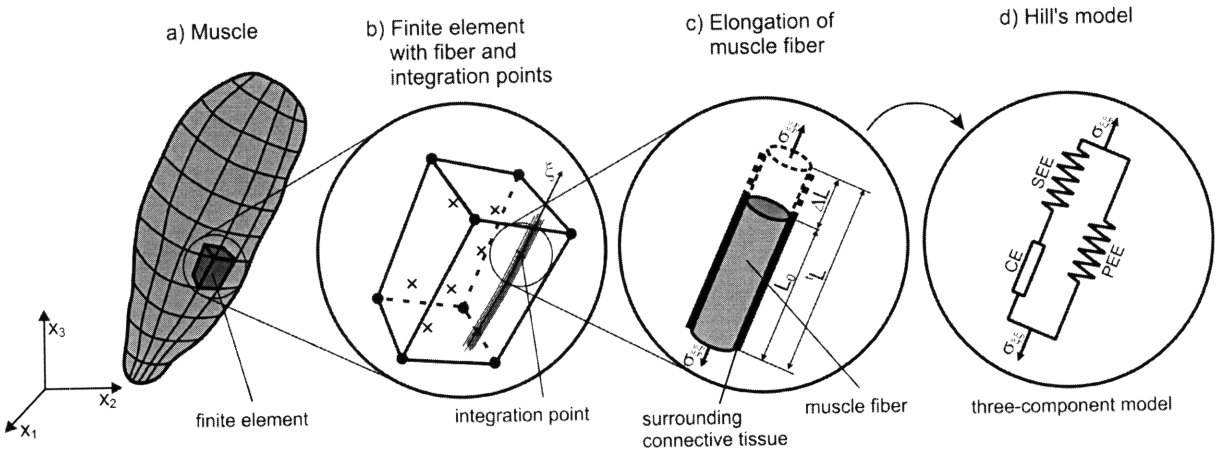

Figure 3.1.A. A schematic of finite element modeling of the muscle, in increasing detail. (a) Dividing the whole muscle as a set of finite elements. (b) Schematic of a finite element with a fiber and internal integration points. (c) Stress leads to fiber elongation. (d) Modeling the fiber using Hill's three-component model.

3.1.2 Preliminary stretch calculation

Before we begin derivation of the stresses and the tangent constitutive matrix, we present the calculation of the stretch for the current configuration of muscle within the incremental-iterative finite element scheme described by equation 3.1.1. The stress and tangent constitutive matrix will be functions of this stretch.

Let ${}^{n+1}\mathbf{x}^{(i-1)}$ specify the last known configuration for the step n and the current iteration i as position vectors of the nodes of the element. We denote the displacements as ${}^{n+1}\mathbf{u}^{(i-1)}$. The desired stretch ${}^{n+1}\lambda^{(i+1)}$ in the fiber direction can be calculated as

$$ {}^{n+1}\lambda^{(i+1)} = \left[\left({}^{0}_{n+1}B_{ij}\, {}^{n+1}\xi_{0i}\, {}^{n+1}\xi_{0j} \right)^{(i-1)} \right]^{-1/2} \qquad (3.1.4) $$

where ${}^{n+1}\xi_{0i}^{(i-1)}$ and ${}^{n+1}\xi_{0j}^{(i-1)}$ are components of the unit vector ${}^{n+1}\xi_{0}^{(i-1)}$, and ${}_{n+1}{}^{0}B_{ij}^{(i-1)}$ are the components of the inverse left Cauchy-Green deformation tensor ${}_{n+1}{}^{0}\mathbf{B}_{ij}^{(i-1)}$. This tensor can be calculated from the inverse deformation gradient tensor ${}_{n+1}{}^{0}\mathbf{F}^{(i-1)}$:

$$ {}_{n+1}{}^{0}\mathbf{B}_{ij}^{(i-1)} = \left({}_{n+1}{}^{0}\mathbf{F}^{T} \, {}_{n+1}{}^{0}\mathbf{F} \right)^{(i-1)} \tag{3.1.5} $$

In turn, the inverse deformation gradient tensor ${}_{n+1}{}^{0}\mathbf{F}^{(i-1)}$ can be calculated using the displacements ${}^{n+1}\mathbf{u}^{(i-1)}$ (here separated into components with subscripts i and j, where $\delta_{ij} = 1$ if $i = j$):

$$ {}_{n+1}{}^{0}F_{ij}^{(i-1)} = \delta_{ij} - \frac{\partial\left({}^{n+1}u_{i}^{(i-1)}\right)}{\partial\left({}^{n+1}x_{j}^{(i-1)}\right)} \tag{3.1.6} $$

To calculate the derivatives, we must use interpolation of the displacements (again separated into components):

$$ \frac{\partial\left({}^{n+1}u_{i}^{(i-1)}\right)}{\partial\left({}^{n+1}x_{j}^{(i-1)}\right)} = \sum_{k=1}^{N} \frac{\partial N_{k}}{\partial\left({}^{n+1}x^{(i-1)}\right)} {}^{n+1}U_{i}^{k(i-1)} \tag{3.1.7} $$

Here N_k are the interpolation functions and ${}^{n+1}U_{i}^{k(i-1)}$ are the components of the nodal displacements.

3.2 Hill's model

For years, the mechanical behavior of muscles has been studied extensively. In 1938, Hill proposed a model for the contraction of muscle based on his own experiments.

This model has lasted for seventy years, and numerous researchers have added ideas to this model. The basic, and most important equation describing muscle mechanics is the aptly named Hill's equation, which describes tetanized skeletal muscle (Hill, 1938):

$$(v+b)(T+a)=b(T_0+a) \tag{3.2.1}$$

In this equation, T represents the tensional force in the muscle, and v represents the velocity of the muscle's contraction. T_0, a constant, is the maximum force developed in the muscle under isometric conditions, and is a function of the muscle length L_0 while a and b are also constants. Hill's equation can be rearranged to a dimensionless form, where the constant $c=\frac{T_0}{a}$ and the maximum muscle velocity $v_0=\frac{bT_0}{a}$:

$$\frac{T}{T_0}=\frac{1-(v/v_0)}{1+c(v/v_0)} \tag{3.2.2}$$

The contractile element (CE) described by Hill's equation is shown in figure 3.2.A (and in part (d) of figure 3.1.A). It is described by Hill's equation, and its tension-length relationship is given by Gordon's curve (Gordon 1966). The CE is alongside two elastic elements, one connected in series (SEE) and the other connected in parallel (PEE). This figure represents Hill's three-element model. The tension-stretch relationship for the SEE is non-linear and given by

$$S=\left(S^*+\beta\right)e^{\left(\alpha\left(\lambda-\lambda^*\right)\right)}-\beta \tag{3.2.3}$$

where α and β are material constants. The PEE is a linear elastic element that models surrounding connective tissue. We will revisit these elements and equations in the next section, section 3.3.

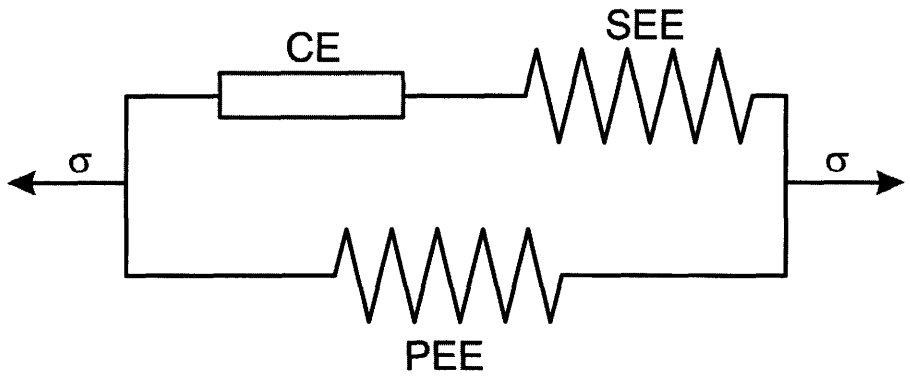

Figure 3.2.A. Hill's three-component model.

3.3 Calculating stress in the direction of muscle fibers

3.3.1 Length relation

To calculate stress in the fiber direction we begin with the geometry shown in figure 3.3.A. (The PEE is not shown in the figure). From the figure, we obtain the following relation:

$$L_{p0}+{}^{0}U_{p} = L_{m0}+{}^{0}U_{m} + L_{s0}+{}^{0}U_{s} \tag{3.3.1}$$

where the variables L_{p0}, L_{m0}, and L_{s0} are the respective initial lengths of the parallel elastic, contractile, and serial elastic elements. (L_{p0} is also the total length). Correspondingly, ${}^{0}U_{p}$, ${}^{0}U_{m}$, and ${}^{0}U_{s}$ are the initial elongations of the parallel elastic, contractile, and serial elastic elements, and in our case are taken to be zero. (We have also, for section 3.3, dropped the use of the ξ notation for the local fiber direction for clarity.)

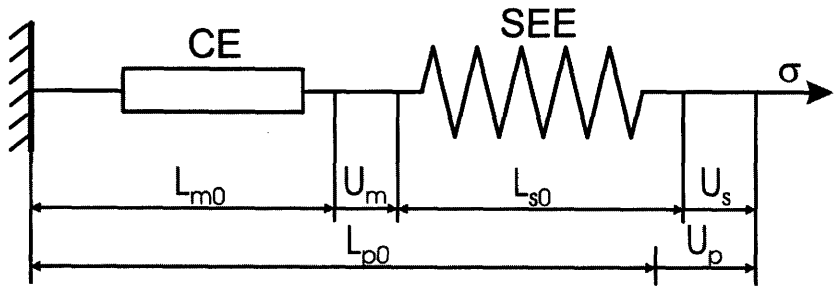

Figure 3.3.A. Geometry of length and elongations in Hill's three-component model.

Now let the constant muscle parameter k represent the ratio of the initial length of the serial elastic element to the length of the contractile element:

$$k = \frac{L_{s0}}{L_{m0}} \tag{3.3.2}$$

We divide the first equation by L_{m0} and rewrite in terms of k and the initial stretches to obtain

$$^0\lambda_m = (1+k)\,^0\lambda_p - k \tag{3.3.3}$$

We take the undeformed configuration to be the initial state, so $^0\lambda_m = 1$ and $^0\lambda_p = 1$.

Similarly, at an arbitrary time t we have the following relations between the lengths and elongations:

$$\begin{aligned} {}^tL_p &= L_{p0} + {}^tU_p \\ &= L_{m0} + {}^0U_m + \int_{t_a}^{t} v_m\,dt + L_{s0} + {}^tU_s \end{aligned} \tag{3.3.4}$$

where v_m is the rate of change of the muscle's length and t_a is the time at which the muscle is activated. Again dividing by L_{m0} and substituting k, we obtain

$$(1+k)^{t}\lambda_p = {}^{0}\lambda_m + \int_{t_a}^{t} \frac{v_m}{L_{m0}} dt + k^{t}\lambda_s \tag{3.3.5}$$

At the end of a given time step, this can be written with increments of stretches $\Delta\lambda_m$ and $\Delta\lambda_s$ as

$$(1+k)^{n+1}\lambda_p = {}^{n}\lambda_m + \Delta\lambda_m + k^{n}\lambda_s + k\Delta\lambda_s \tag{3.3.6}$$

3.3.2 Stress increment of serial elastic element

Furthermore, the stresses σ_m and σ_s in the contractile and serial elastic elements must be equal for all times. Therefore,

$${}^{n+1}\sigma_m = {}^{n+1}\sigma_s \tag{3.3.7}$$

Now we use Hill's equation (equation 3.2.2) from the previous section to obtain

$${}^{n+1}\sigma_m = {}^{n}\sigma_0 \, {}^{n+1}\alpha_a \frac{1+\Delta\lambda_m/\Delta\lambda_{m0}}{1-c(\Delta\lambda_m/\Delta\lambda_{m0})} \tag{3.3.8}$$

where $v/v_0 = \Delta\lambda_m/\Delta\lambda_{m0}$, and ${}^{n+1}\alpha_a$ is the activation function of the muscle (not to be confused with the constant α in the SEE tension-stretch relationship). The value ${}^{n}\sigma_0$ is obtained from Gordon's curve and corresponds to the stretch ${}^{n}\lambda_m$. We calculate the value $\Delta\lambda_{m0}$ as

$$\Delta\lambda_{m0} = \Delta t(\dot{\lambda}_{m0}) \tag{3.3.9}$$

where $\dot{\lambda}_{m0}$ is the strain rate corresponding to maximum isometric tetanized force, and is considered to be a known characteristic of the contractile element. (Also, note the change

of sign in the fraction, which comes as a result of Hill's equation describing contraction. The contraction velocity is taken to be negative, so we change signs.)

The activation function, which is dependent on time, is what we seek to reveal through simulation experiments. It is a scaling factor for stress with respect to the tetanized state, and varies between 0 and 1. The passive, non-activated state corresponds to $\alpha_a = 0$, while the fully tetanized state corresponds to $\alpha_a = 1$.

Using the tension-stretch relationship for the serial contractile element (equation 3.2.3), we now can find the constitutive equation for the stress:

$$\begin{aligned} {}^{n+1}\sigma_s &= \beta\left(e^{\alpha\left({}^{n}\lambda_s - 1 + \Delta\lambda_s\right)} - 1\right) \\ &= e^{\alpha\Delta\lambda_s}\left({}^{n}\sigma_s + \beta\right) - \beta \end{aligned} \tag{3.3.10}$$

In this equation we have written the stress corresponding to the start of the time step as

$${}^{n}\sigma_s = \beta\left(e^{\alpha\left({}^{n}\lambda_s - 1\right) - 1}\right) \tag{3.3.11}$$

We can rearrange the length equation at the end of a time step (equation 3.3.6) to get

$$\Delta\lambda_m = a_1 - k\Delta\lambda_s \tag{3.3.12}$$

where

$$a_1 = (1+k)^{n+1}\lambda_p - {}^{n}\lambda_m - k\,{}^{n}\lambda_s \tag{3.3.13}$$

Combining equations 3.3.7, 3.3.8, 3.3.10, and 3.3.12 we obtain this equation

$$f(\Delta\lambda_s) = (a_2 + a_3\Delta\lambda_s)e^{\alpha\Delta s} + a_4\Delta\lambda_s + a_5 = 0 \tag{3.3.14}$$

with coefficients

$$a_2 = \left({}^n\sigma_s + \beta\right)\left(1 - \frac{a_1 c}{\Delta\lambda_{m0}}\right)$$
$$a_3 = \left({}^n\sigma_s + \beta\right)\frac{kc}{\Delta\lambda_{m0}}$$
$$a_4 = k\frac{{}^n\sigma_0{}^{n+1}\alpha_a - \beta c}{\Delta\lambda_{m0}}$$
$$a_5 = {}^n\sigma_0{}^{n+1}\alpha_a - \beta - a_1\frac{{}^n\sigma_0{}^{n+1}\alpha_a - \beta c}{\Delta\lambda_{m0}} \tag{3.3.15}$$

The stretches and stresses at the start of any time step are known, and the total sarcomere stretch can be calculated from displacements. Thus all of the coefficients $a_1 \cdots a_5$ are known. Hence, this non-linear equation has only one unknown quantity, the stretch increment $\Delta\lambda_s$, and can be solved by Newton's method. With the stretch increment we can determine the stress in the serial elastic element for the next step.

3.3.3 Calculating stress in the parallel elastic element

The only component of the total stress left to calculate is that of the parallel elastic element. If we assume the surrounding connective tissue that the PEE represents is a linear elastic isotropic medium, we can calculate the stress using this relation

$${}^{n+1}\boldsymbol{\sigma}^E = \mathbf{C}^{E\,n+1}\mathbf{e} \tag{3.3.16}$$

where $\mathbf{C}^E$ is the elastic constitutive matrix, and ${}^{n+1}\mathbf{e}$ is the strain at a material point, which can be determined from displacements.

3.3.4 Total stress

The total stress in the element can be expressed as

$$^{n+1}\boldsymbol{\sigma} = \boldsymbol{\sigma}_s\phi + {}^{n+1}\boldsymbol{\sigma}^E(1-\phi) \tag{3.3.17}$$

where ϕ is the fraction of muscle fibers (the active fraction of muscle, represented by the series element and contractile element) in the total muscle volume. The quantity $(1-\phi)$ therefore represents the fraction of inactive muscle represented by the parallel elastic element. Note that the total stress refers to the local coordinate system where one axis is in the direction of the muscle element. A tensor transformation must be implemented to obtain stress in the overall structure's coordinate system (Cartesian, cylindrical, etc.).

3.4 Calculating the tangent constitutive matrix

The tangent constitutive matrix $^{n+1}\mathbf{C}$ (Kojic and Bathe, 2005) of the muscle as a continuum can be calculated in an analogous manner to the total stress using the fraction of active muscle ϕ:

$$^{n+1}\mathbf{C} = \frac{\partial\left(^{n+1}\boldsymbol{\sigma}\right)}{\partial\left(^{n+1}\mathbf{e}\right)} = (1-\phi)\mathbf{C}^E + \phi\frac{\partial\left(^{n+1}\boldsymbol{\sigma}_s\right)}{\partial\left(^{n+1}\mathbf{e}\right)} \tag{3.4.1}$$

This formulation corresponds to the global coordinate system, but we can only determine the derivatives in the local coordinate system of the fiber. Instead we form the local tangent constitutive matrix $^{n+1}\overline{\mathbf{C}}$ whose terms are:

$$
\begin{aligned}
{}^{n+1}\overline{C}_{11} &= (1-\phi)C_{11}^{E} + \phi\frac{\partial\left({}^{n+1}\sigma_s\right)}{\partial\left({}^{n+1}e_{\xi\xi}\right)} \\
{}^{n+1}\overline{C}_{ij} &= (1-\phi)C_{ij}^{E} \text{ for other } i,j
\end{aligned}
\tag{3.4.2}
$$

Here, C_{ij}^{E} are elastic matrix terms of the surrounding connective tissue, and $e_{\xi\xi} = L/L_0$, represents the fiber strain. (Recall that L and L_0 are the current and initial length of the fiber, respectively.)

Now we show how to calculate the derivative $\frac{\partial\left({}^{n+1}\sigma_s\right)}{\partial\left({}^{n+1}e_{\xi\xi}\right)}$. Recalling that $\lambda = \lambda_p$ (since the parallel element is the whole length of the element) is a function of L/L_0, we can write

$$
\frac{\partial\left({}^{n+1}\sigma_s\right)}{\partial\left({}^{n+1}e_{\xi\xi}\right)} = \lambda_p\frac{\partial\left({}^{n+1}\sigma_s\right)}{\partial\left({}^{n+1}\lambda_p\right)}
\tag{3.4.3}
$$

Using equation 3.3.10, we can get

$$
\frac{\partial\left({}^{n+1}\sigma_s\right)}{\partial\left({}^{n+1}\lambda_p\right)} = \alpha\left({}^{n}\sigma_s + \beta\right)e^{\alpha\Delta\lambda_s}\frac{\partial\Delta\lambda_s}{\partial\left({}^{n+1}\lambda_p\right)}
\tag{3.4.4}
$$

Now, we have yet another unknown derivative $\frac{\partial\Delta\lambda_s}{\partial\left({}^{n+1}\lambda_p\right)}$ to calculate. This derivative can be calculated by differentiating the non-linear equation (3.3.14) with coefficients given in equations 3.3.15 from the previous section 3.3 with respect to ${}^{n+1}\lambda_p$, obtaining

$$
\frac{\partial f(\Delta\lambda_s)}{\partial\left({}^{n+1}\lambda_p\right)} = (k_2 + a_3x)e^{\alpha\Delta\lambda_s} + (a_2 + a_3\Delta\lambda_s)\alpha e^{\alpha\Delta\lambda_s}x + a_4x + k_5 = 0
\tag{3.4.5}
$$

where x represents the unknown derivative $\frac{\partial \Delta\lambda_s}{\partial\left({}^{n+1}\lambda_p\right)}$, and

$$\frac{\partial a_1}{\partial\left({}^{n+1}\lambda_p\right)} = 1 + k$$

$$\frac{\partial a_2}{\partial\left({}^{n+1}\lambda_p\right)} = -\left({}^{n}\sigma_s + \beta\right)\left(\frac{c}{\Delta\lambda_{m0}}\frac{\partial a_1}{\partial\left({}^{n+1}\lambda_p\right)}\right)$$

$$\frac{\partial a_3}{\partial\left({}^{n+1}\lambda_p\right)} = -\frac{a_4}{k}\frac{\partial a_1}{\partial\left({}^{n+1}\lambda_p\right)} = k_5 \tag{3.4.6}$$

We back-substitute $\frac{\partial \Delta\lambda_s}{\partial\left({}^{n+1}\lambda_p\right)}$ to get $\frac{\partial\left({}^{n+1}\sigma_s\right)}{\partial\left({}^{n+1}\lambda_p\right)}$, which then allows us to calculate $\frac{\partial\left({}^{n+1}\sigma_s\right)}{\partial\left({}^{n+1}e_{\xi\xi}\right)}$. This finally lets us calculate the tangent constitutive matrix.

4 DTI imaging and tractography

DTI tractography derives the orientation of local fiber populations in tissue by measuring anisotropic proton diffusion within tissue (Basser et al, 1994; Wedeen et al, 2001). The physical basis by which diffusion weighted MRI infers fiber direction in muscular tissue has been previously published (Wedeen *et al.*, 2001; Napadow *et al.*, 2001, Gilbert *et al.*, 2006a; Gilbert *et al.*, 2006b, Gaige *et al.*, 2007) and validated relative to microscopic visualization (Napadow *et al.*, 2001). In brief, diffusion represents the random translational motion of water molecules in biological tissue and is principally modulated by the presence and location of macromolecular barriers to water displacement. Thus the preferential motion in the direction of myofibers provides the basis for deducing 3D fiber alignment. The diffusion tensor depicts net proton diffusion in a volume of tissue with a symmetric 2nd rank tensor, and can be interpreted as an ellipsoid whose axes are constructed along its three orthogonal eigenvectors with each axis proportional to its eigenvalues. The application of gradients, configured as evenly spaced directions on the surface of a model sphere, results in a system of linear equations that over-constrains the components of the diffusion tensor and may be solved using multiple linear regression. Diffusion weighted gradients were applied in 90 unique directions employing single shot echo-planar (EPI) spatial encoding and the following imaging parameters: TR = 3000 ms, TE = 80 ms, field of view 192 mm x 192 mm, 3 mm slice thickness, and a b-value of 500 s/mm2. These parameters allowed complete acquisitions for the DTI tractography image set to be accomplished in approximately 5 minutes. Maximum diffusion is a vector defined as the largest eigenvector of the diffusion tensor.

We now use the DTI data to generate multi-voxel myofiber tracts along the maximum diffusion vector per voxel, employing streamline construction, a method for constructing connections along the vector directions in a vector field (Gilbert *et al.*, 2006b). The specific method operates by applying the constraint that a certain angular threshold must be met to establish intervoxel connectivity, and thus constitute the myofiber tract. In the current work, if the angular difference between a given streamline and the maximum diffusion vector of an adjacent voxel is less than 35 degrees, intervoxel myofiber tract continuity is established.

5 Mesh generation and simulation via PAK-S and Musculo

One of the central assumptions behind the mesh is that it is composed of two materials, a collagen-like material and a muscle fiber-like material. The collagen material is assumed to be isotropic and not subject to activation, functioning instead as a sliding element between elements composed of muscle. Muscle fibers are assumed to be anisotropic and contract according to Hill's model (described above). From a single-voxel thick tractographic image derived from DTI, a 2D mesh was generated in order to approximate lingual anatomy during the propulsive phase of swallowing. Specifically, myofiber tracts resolved in 3D were projected onto the plane representing the midline of the tongue. Elements were determined according to these myofiber projections. The resolution of the myofiber tracts was approximated as a single voxel width, and thin collagen elements were generated between neighboring myofiber tract elements.

In a practical sense, there unfortunately is no way to automatically generate a mesh that satisfies the directionality constraints imposed on its internal geometric structure. Therefore, the mesh was developed by hand, by sampling the tractographic image. These samples provided the basis for nodes in the mesh, and these nodes were connected to form the muscle fiber and collagen elements. Pixel coordinates were translated to absolute coordinates in millimeters, given knowledge of the resolution and voxel size (3 mm) in the original DTI image; the final size of the tongue mesh is approximately 6.5 cm square. The mesh is shown in figure 5.A.

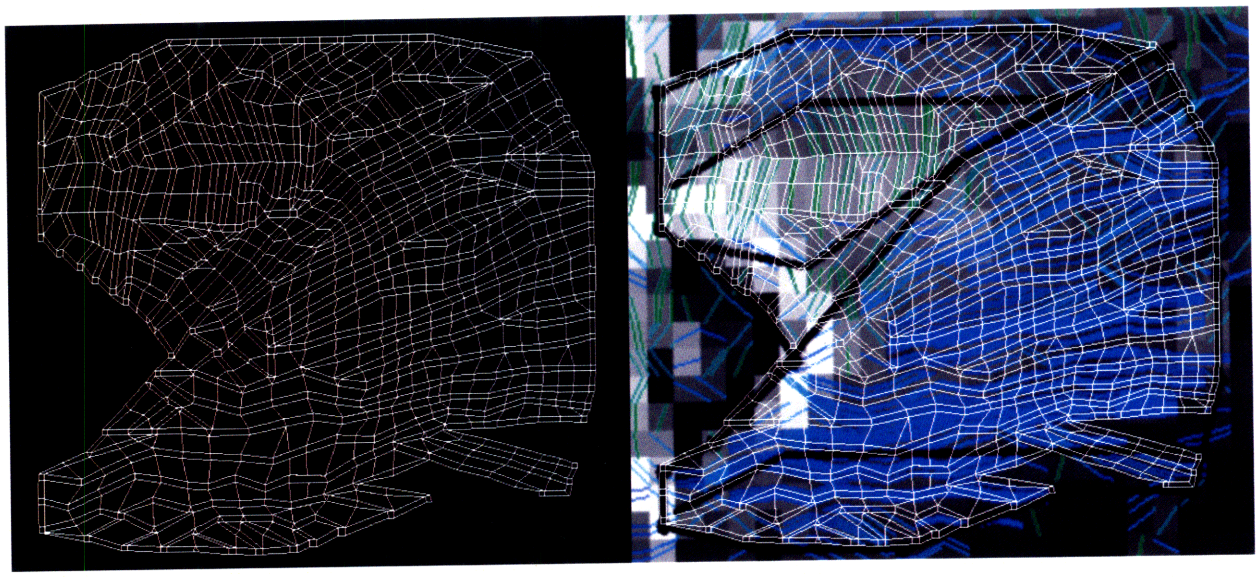

Figure 5.A. The mesh derived from DTI data. Left: the mesh alone. Right: the mesh overlaid on the original DTI image slice. The black lines indicate approximate muscle fiber groups.

The activation and subsequent movement of the tongue were simulated over 500 milliseconds in 50 equally spaced steps (10 ms per step). Simulation was performed using the Windows command line simulation package PAK-S, which applies the Hill's model described in Section 3 to our mesh. PAK-S output was viewed in its companion program Musculo. We constrained the movement of the corner nodes in the front of the tongue during the simulation in order to model connectivity of the tongue to the palate. In initial simulations we did not pre-deform the tip of the tongue upwards. However, we later revised the simulation to do so as some contractions were not possible without the simulation of crossing myofibers. Ruby scripts were also used to assist in troubleshooting of the simulation process.

For the full collagen elements, we assigned a Young's modulus of 0.5 MPa and a Poisson ratio of 0.5. With regards to the muscle finite elements, for the parallel elastic element, we used a Young's modulus of 1.0 MPa and Poisson ratio of 0.45, reflecting the

near incompressibility of the tongue. The constants α and β were 9.4 and 0.11 MPa respectively for the series elastic element. We chose the constants k and a to be 0.3 and 0.07 MPa. The initial strain rate λ_m of the contractile element was 2 m/s. Since we were modeling some connective tissue outside of the Hill's model context, we set the fraction ϕ of active muscle in the muscle elements to be relatively high, at 0.9. Finally, the maximum tetanized isometric stress was 0.22 MPa.

While activation functions in the Hill's model cannot be measured directly, they can be derived given displacement values and the known material properties of the muscle and collagen. The activation functions were determined iteratively and compared with the local strain function ascertained employing gated phase contrast MRI in Felton *et al.* (2007, 2008) and global deformation during the propulsive phase of swallowing. We attempted to define these activation functions over different areas of the tongue so that they qualitatively reproduced such movement.

6 Results

Our resulting mesh recapitulated the myofiber structures of the tongue very closely (figure 5.A, above). In figure 6.A we further show how the mesh and DTI tractography image compare with anatomical features in the tongue.

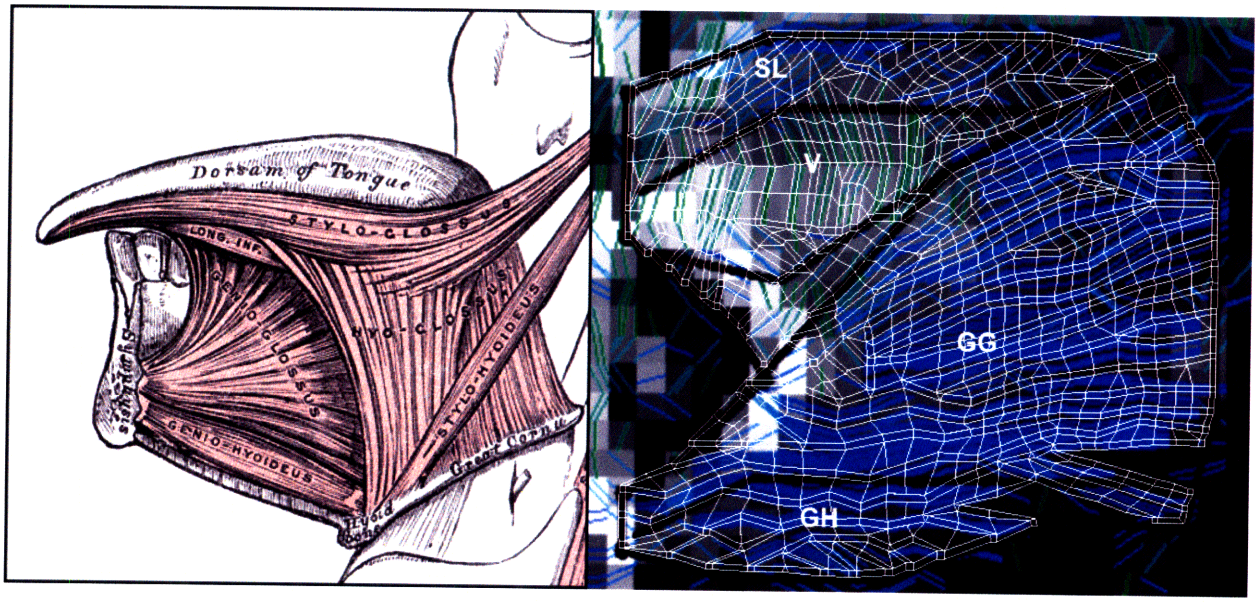

Figure 6.A. Mesh and DTI tractography compared with anatomy. The left figure is obtained from Gray's Anatomy (Gray, 1918). Since this is a midline sagittal slice, not all muscles in the tongue are visible. On the right-hand side we have labeled the geniohyoid (GH), genioglossus (GG), and verticalis (V). Notably invisible are the styloglossus and hyoglossus.

In our simulation, we were able to reproduce the dipping of the posterior of the tongue seen by Felton *et al* (2008). Despite the close adherence of the mesh to the tongue structure within the midline plane, we were unable to find activation functions that led to the deformation of the tip of the tongue upwards, for bolus accommodation. Therefore, as

mentioned in section 5, we pre-deformed the tip of the tongue upwards. Figure 6.B. shows this pre-deformation.

After this adjustment, we were able to find activation functions that did force the tip of the tongue to move in the posterior direction, thereby reproducing the gross motion in later part of bolus accommodation and early propulsive motion. However, our motion is less pronounced (also figure 6.B).

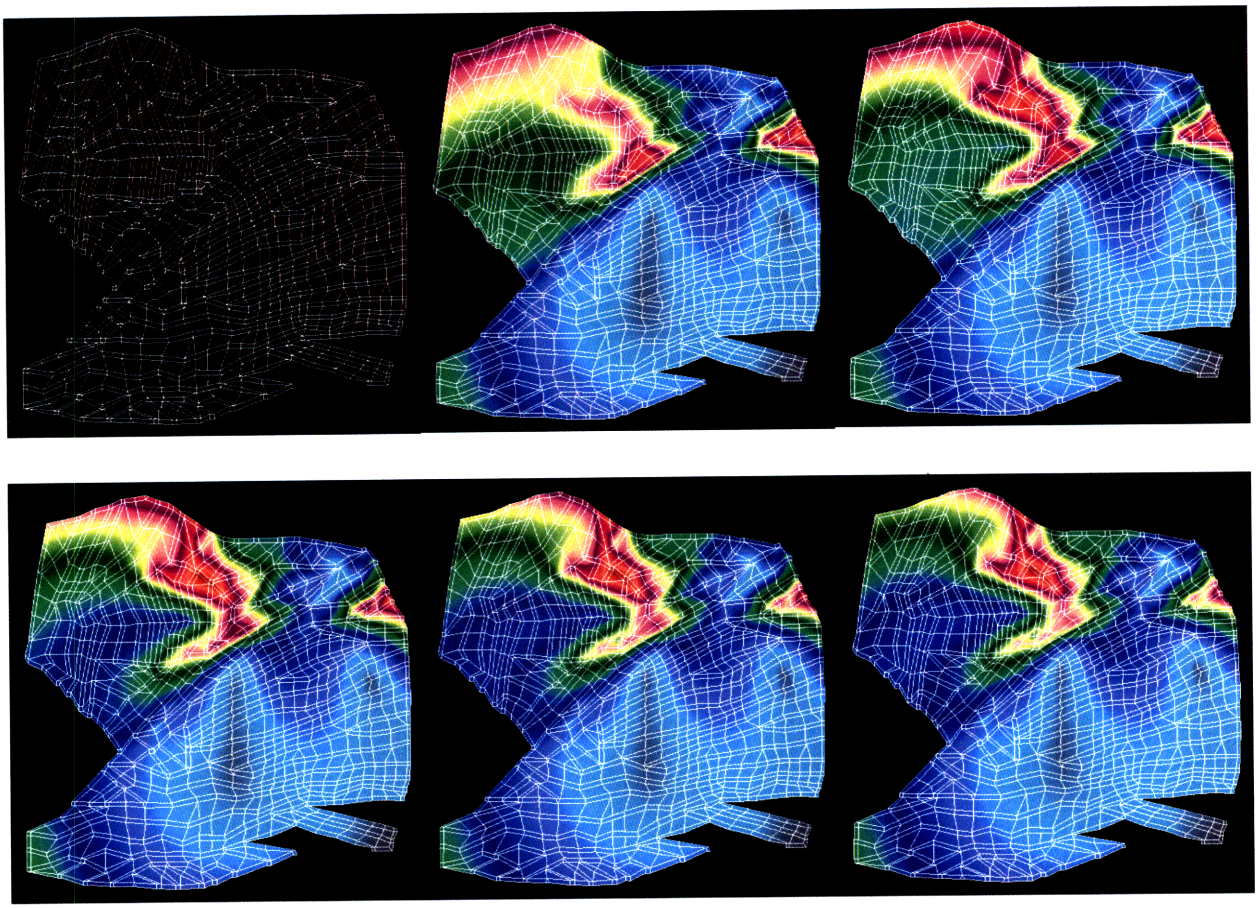

Figure 6.B. Deformation of the tongue during simulation. Top row, from left to right: tongue before activation (pre-deformed), tongue after 100 ms and 200 ms. Bottom row, from left to right: tongue after 300 ms, 400 ms, and 500 ms. Refer to figure 6.C for the areas activated.

Finally, the activations that we found that produced such motion are shown in figure 6.C. We activated a portion of the verticalis, but most of the activation can be seen to come from the genioglossus.

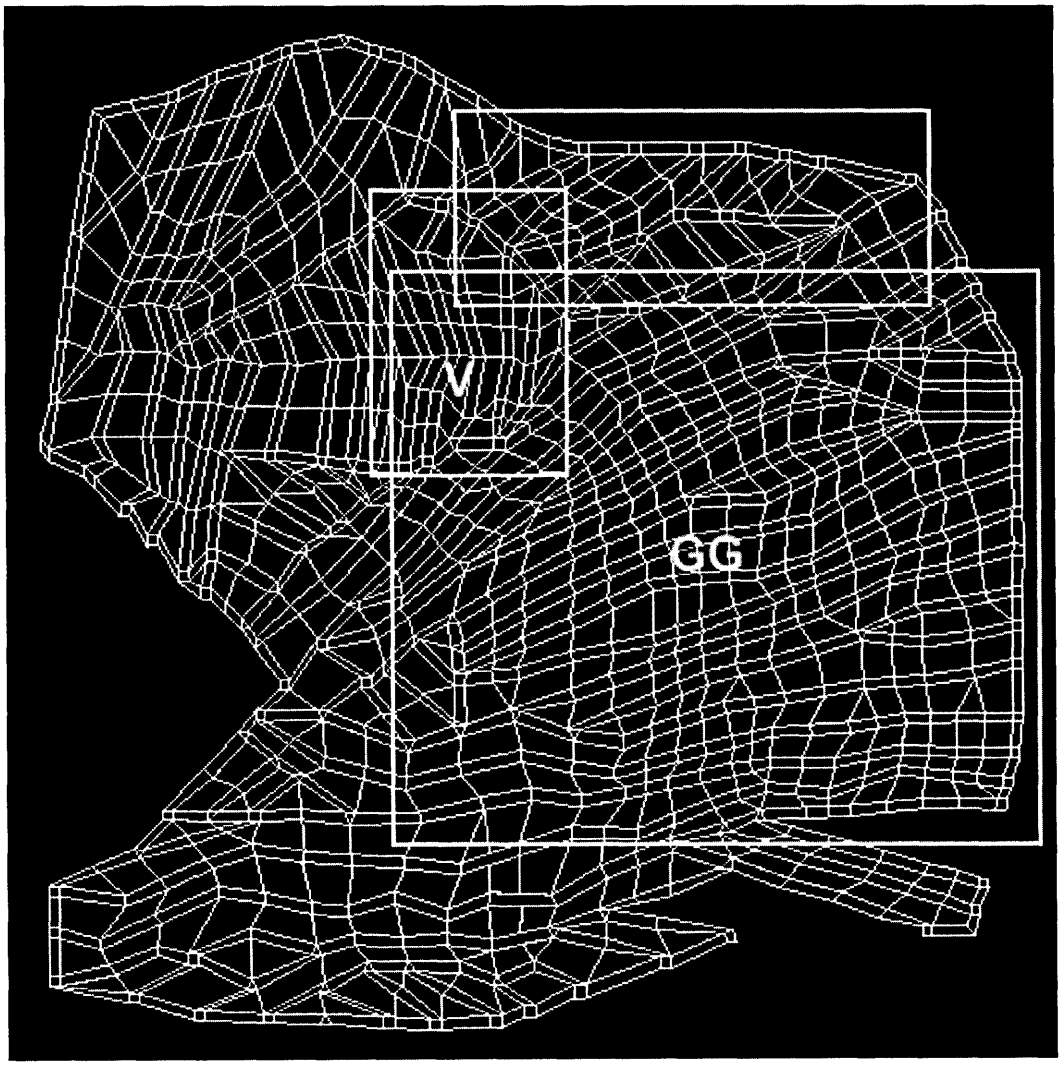

Figure 6.C. Activated muscles in the tongue. Boxed areas were subject to activation, with a peak activation function amplitude of 1 between 300 and 500 ms.

7 Discussion

We have demonstrated that it is possible to deduce activations that reproduce given deformations in the tongue using a finite element model derived from DTI and tractography data. Additionally, the fact that various activation functions were required to produce realistic movement even in the plane supports the idea that propulsive lingual deformation is a synergistic process involving many muscles in the tongue. Still, our model can be improved in several ways.

7.1 Improvements to the model

It is vital that the activation functions are as correct as possible. Determining the correct activation functions in a healthy tongue would allow us to produce disease models of the tongue, where the mesh and associated material properties reflect atrophied or otherwise malfunctioning areas of the tongue with the same activation functions. Reproducing the correct displacement is an indicator that the activation functions are also approximately correct. While obtaining the correct tongue movement is a decent form of validation, ideally, we would also be able to validate against a second data set from a diseased or atrophied tongue using the same activation functions.

We would also like to find a more quantitative method of validating our simulation results. One possible method would be to reproduce internal strain accurately as well, as the correct displacement can be produced by multiple sets of activation functions. While internal strain cannot be measured physically, our group has previously demonstrated a way for deducing such strains (Felton et al. 2008).

The tongue is an ideal model for initial studies because it is relatively regular in shape, with symmetric fiber distribution. Therefore, our two-dimensional model of the midline of the tongue is immediately relevant to the rest of the tongue, and mostly accurate for simple tongue motions. In reality, however, there are still elements of lingual architecture that are lost when we project the tracts onto two dimensions. For example, with a simple 2D model one is unable to model the deformations caused by crossing fibers, which are the fibers that come in or out of the plane of our simulation, and which are not visible in our single-voxel slice. By focusing on the midline, we have also lost key muscles not entirely associated with the midline of the tongue, such as the hyoglossus, which provides important support that we instead provide with fixed nodes, or the styloglossus, which may be involved in pulling the tongue back to accommodate the bolus. This forced us to pre-deform the tongue to obtain an accurate simulation, again underlining the importance of having as complete a model as possible.

Initially we did try to model a thin three dimensional slice approximately three voxels thick, but were unable to do so due to computational difficulties related to mesh generation. As previously noted, there is no mesh generation algorithm that can maintain the required internal structure prescribed by the tractography data. This forced us to generate our initial mesh by hand, which, while time-consuming and occasionally buggy, was at least possible. Generating a three-dimensional mesh by hand would definitely be out of the question. Thus, in future work, we must develop an algorithm that produces meshes of high quality, taking into account the full three-dimensional qualities of the tongue.

The FEM described here can be applied to other organs such as the heart, esophagus, and rectum. However, these organs are significantly more complex than the tongue, and contain more types of tissue than simply collagen and muscle. Even for the tongue, the assumption of collagen and muscle is a slight simplification. Therefore, in future models, different types and more properties of biological materials must be modeled. For example, stiffness of materials cannot be directly specified in the current version of PAK-S.

7.2 Usability and surgical planning

One of the long-range goals of this work is to produce surgical planning tools. Since DTI can show diseased or atrophied myofiber tracts, meshes for diseased organs can be easily derived from that data, and the effects of atrophy simulated from those meshes. (how? Can DTI pick up the damaged areas? According to Teresa's work yes, need more detail)

However, many improvements need to be made to the software and the simulation workflow for this tool to be useful to the medical community. First and foremost, the simulation software PAK-S, while robust, would present a significant usability hurdle for the average medical professional who is not well-versed in the finer points of finite element analysis. There is no interactive mesh generation, and error messages due to malformed meshes are terse and sometimes uninformative (as they are for many other command line programs). The workflow is inefficient as one has to keep switching between mesh input file, simulation and viewing. Documentation for the software is somewhat poor as it has not been updated even after numerous updates to incorporate the non-linear stress-strain models used for this research.

Second, even after overcoming the usability problems, most medical professionals are not trained in the finer details of finite element modeling, and do not have the time to fine tune a mesh to perfection. Therefore, the system must be as close to a "black box" as possible. Again, this will require significant advances in mesh generation automation and quality, as described above. In this way medical professionals can harness the power of our model with just a few clicks after performing a DTI scan.

In summary, we have found that DTI and tractography allows us to produce a high quality, detailed mesh for finite element analysis. We demonstrated that the model presented here, combining the imaging power provided by DTI and tractography with a powerful finite element method based on Hill's model can recapitulate deformation during the propulsive phase of swallowing. With further refinement from the biological, computational, and even usability point of view, this tool has the potential to be a significant advance that opens the door for many applications.

8 References

Basser PJ, Mattiello J, LeBihan, D (1994). MR diffustion tensor spectroscopy and imaging. *Biophys J* 66: 259-267.

Felton SM, Gaige TA, Reese TG, Wedeen VJ, Gilbert RJ (2007). Mechanical basis for lingual deformation during the propulsive phase of swallowing as determined by phase-contrast magnetic resonance imaging. *J Appl Physiol* 103: 255-265.

Felton SM, Gaige TA, Benner T, Wang R, Reese TG, Wedeen VJ, Gilber RJ (2008). Associating the mesoscale fiber organization of the tongue with local strain rate during imaging. *J Biomech* 41: 1782-1789.

Gaige TA, Benner T, Wang R, Wedeen VJ, Gilbert RJ (2007). Three dimensional myoarchitecture of the human tongue determined in vivo by diffusion tensor imaging with tractography. *J Magn Resn Imaging* 26: 654-661.

Gilbert RJ, Magnusson LH, Napadow VJ, Benner T, Wang R, Wedeen VJ (2006a). Mapping complex myoarchitecture in the bovine tongue with diffusion-spectrum magnetic resonance imaging. *Biophys J* 91: 1014-1022.

Gilbert RJ, Wedeen VJ, Magnusson LH, Benner T, Wang R, Dai G, Napadow VJ, Roche KK (2006b). Three dimensional myoarchitecture of the bovine tongue demonstrated by diffusion spectrum imaging with tractography. *Anat Rec A Discov Mol Cell Evol Biol* 288: 1173-1182.

Gilbert RJ, Napadow VJ, Gaige TA, Wedeen VJ (2007). Anatomical basis of lingual hydrostatic deformation. *J Exp Biol* 210: 4069-4082.

Gordon AM, Huxley AF, Julian FJ (1966). The variation in isometric tension with sarcomere length in vertebrate muscle fibres. *J Physiol* 184: 170-192.

Gray H (1918). *Anatomy of the Human Body*, online version. Available at http://www.bartleby.com/107. Last accessed 22 August 2008.

Hill AV (1938). The heat of shortening and the dynamic constants of muscle. *Proc R Soc London B Biol Sci* 126: 136-195.

Jordan CE (1996). Coupling internal and external mechanics to predict swimming behavior: a general approach. *Am Zool* 36: 710-722

Kristan WB, Skalak R, Wilson RJA, Skierczynski BA, Murray JA, Eisenhart FJ, Cacciatore TW (2000). Biomechanics of hydroskeletons: lessons learned from studies of crawling in the medicinal leech. In *Biomechanics and Neural Control of Posture and Movement*, ed Winters J and Crago P, pp 206-218. New York: Springer-Verlag.

Kojic M, Mijailovic S, Zdravkovic N (1998). Modelling of muscle behaviour by the finite element method using Hill's three-element model. *Int J Numer Meth Eng* 43: 941-953.

Kojic M, Bathe KJ (2005). *Inelastic Analysis of Solids and Structures.* Berlin-Heidelberg: Springe-Verlag.

McLean MR, Prothero J (1987). Coordinated three-dimensional reconstruction from serial sections at macroscopic and microscopic levels of resolution: the human heart. *Anat Rec* 219: 434-439.

McLean MR, Prothero J (1992). Determination of relative fiber orientation in heart muscle: methodological problems. *Anat Rec* 232: 459-465.

Napadow VJ, Chen Q, Mai V, So PT, Gilbert RJ (2001). Quantitative analysis of three-dimensional-resolved fiber architecture in heterogeneous skeletal muscle tissue using NMR and optical imaging methods.

Napadow VJ, Kamm RD, Gilbert RJ (2002). A biomechanical model of sagittal tongue bending. *J Biomech Eng* 124: 547-556.

Skierczynski BA, Wilson RJA, Kristan WB, Skalak R (1996). A model of the hydrostatic skeleton of the leech. *J Theor Biol* 181: 329-342.

Stejskal EO (1965). Use of spin echoes in a pulsed magnetic field gradient to study anisotropic, restriced diffusion and flow. *J Chem Phys* 43: 3597-3603.

Van Leeuwen JL, Kier WM (1997). Functional design of tentacles in squid: linking sarcomere ultrastructure to gross morphological dynamics. *Philos Trans R Soc Lond B Biol Sci* 352: 551-571.

Weeden VJ, Reese TG, Napadow VJ, Gilbert RJ (2001). Demonstration of primary and secondary fiber architecture of the bovine tongue by diffusion tensor magnetic resonance imaging. *Biophys J* 80: 1024-1028.

Wadepuhl M, Beyn WJ (1989). Computer simulation of the hydrostatic skeleton. The physical equivalent, mathematics and application to worm-like forms. *J Theor Biol* 136: 379-402.

Wilson JF, Mahajan U, Wainwright SA, Croner LJ (1991). A continuum model of elephant trunks. *J Biomech Eng* 113: 79-84.